Flexural Behavior of A Novel high-strength RCFST Column-to-Column Connection

Ben. Mou[1,3], Yingze. Li[1], Fangying. Wang[2], Wei Pan[3], Yong Zhao[1]

[1] iSMSRT, Qingdao University of Technology, Qingdao 266033, China

[2] School of Civil and Environmental Engineering, Nanyang Technological University, Singapore

[3] Department of Civil Engineering, The University of Hong Kong, Hong Kong

Abstract:

Brittle fracture is one of the principal disincentives to limit the use of ultrahigh-strength steels in tall buildings. This paper proposes a novel column-to-column connection without full penetration welding in reinforced concrete-filled steel tubular composite columns. The paper describes an experimental investigation into the flexural behavior of the proposed RCFST column-to-column connection, in which the steel was manufactured using ultrahigh-strength steel grades H-SA700 and USD 685. Four specimens with varying configurations of reinforcing steel bars (separated type or gathered type) and column shapes (square or circular) were tested under four-point bending to evaluate the failure modes, flexural capacity, and deformation capacity. The results show that the gathered type of configuration of reinforcing steel bars can effectively improve the flexural capacities while having a negligible effect on the strain distribution of steel tubes or steel bars. Besides, the column type was found to significantly influence the strain distribution of the steel tube. The design formulae show accuracy and reliability and could be applied to assess the yield and ultimate strength of the proposed new connections.

Keywords: Ultra-high strength steel; Reinforcing concrete filled steel tubular; Flexural capacity; Column to column connection;

1. Introduction

Concrete-filled steel tubular (CFST) sections have numerous well-known structural and constructional benefits over plain concrete or hollow steel tubes [1–4]. The interaction between the steel tube and the concrete infill leads to the efficient utilization of both constituent materials by confining the concrete core and delaying local buckling of the steel tube. This has been sufficiently utilized in CFST columns, where the most favorable properties of the constituent materials have been exploited and thereby greatly improve the strength and ductility of the structural systems. In recent years, with the advantages of light self-weight, great load-bearing capacity, and favorable ductility, the use of CFST columns has become widespread in high rise and large-span construction [5, 6]. An example of the use of CFST columns in an exhibition hall is provided in Fig.1.

The axial, local and eccentric compression behaviors of CFST columns have been extensively examined in Han et al. [7] and Wang et al. [8], respectively, and the formulas for predicting compressive strengths have been established. Moreover, Jiang et al. [9] proposed a bending analysis model of thin-walled CFST for square and rectangular thin-walled CFST with the width-thickness ratio of 50-100. The influence of key variables in CFST beams, such as the local slenderness of the steel tube, the concrete cross-section area, the concrete strength as well as the beneficial restraining effect of the concrete infill on the bending moment capacity and ductility of CFST beams were examined by Chitawadagi et al. [10]. The interaction between the steel tube and the concrete was further verified in a numerical study of rectangular CFST beams by Wang et al. [11]. Moreover, the bond-slip behavior between the steel tube and built-in concrete is also an important factor affecting the bending behavior of CFST columns. Tao et al. [12] investigated the pull-out tests of 24 CFST specimens and the results indicate that the bond strength decreases significantly with the increase of section size and concrete age. Dong et al. [13,14] conducted the pull-out tests on 16 square HSCFSTs and 18 circular HSCFSTs with various configurations and found that the combination of ring ribs and vertical ribs significantly improved the bonding strength and energy dissipation capacity of columns. Alatshan et al. [15] reviewed the influence of internal and external stiffeners on different structural properties of CFST members in the past two decades and revealed that the specimens with stiffeners have been less studied under pure bending. Altogether, the aforementioned investigations have revealed that the variation of various parameters has a significant influence on the bending performance of CFST beams.

At present, butt-welded connection and bolted-flange connection are the two main types of CFST column-column connections, which are used in civil engineering. Lee et al. [16] established two finite element models for butt-welded CHS members. The results showed that welding residual stress had a significant impact on the initial stiffness and ultimate strength of CHS members under bending. Wang et al. [17] conducted the bending test and finite element analysis on 4 column-column joints connected with flange plates and put forward a practical design model. Liu et al. [18] carried out a static test and finite element analysis on 12 column-column bolted-flange connections. The results showed that flange thicknesses had a greater impact on connections performance compared with flange widths and bolt edge distances.

The use of high strength steel allows the structural members to be designed with smaller dimensions, thereby a good economy can be achieved with the reduction of the self-weight and foundation sizes. Recent years have witnessed an increasing upsurge in the application of high strength steel in various structural construction [19,20], and employing high strength steel in composite structures is also attracting increasing attention from international engineers and researchers. Specifically, Gho and Liu [21] conducted pure bending tests on 12 high-strength rectangular CFST specimens and found that all the examined specimens exhibited excellent post-yield performance and ductility. Wang et al. [22] examined the axial compressive behavior and flexural behavior of concrete-filled double-skin tubular columns with high strength steel inner tubes and founded that the use of high strength steel greatly improves the load-carrying capacities of the composite cross-sections. Li et al. [23] conducted six high-strength concrete-filled high-strength square steel tube specimens with varying steel ratios, and the results showed that the specimens with a higher steel ratio characterized by greater ultimate flexural resistance and deformation capacities. Choi et al. [24] tested the rectangular CFT columns with high strength steel HSA800 under weak axis bending and found that the hybrid RCFT sections can enhance the full plastic strength of members. Meanwhile, the bending resistance of CFST sections can also be significantly improved by employing more steel components in the column, such as arranging a certain number of rebars or structural steel angles or I-sections inside the columns [25]. A comparative study of RCFST columns with pure CFST columns also has revealed that RCFST columns exhibit higher strength, stiffness, and ductility, particularly in the post-ultimate stage [26]. To date, research work on concrete-filled tubular structures employing high strength steel has mainly focused on either column members or beam members, with few experimental data on the member connections, which are deemed to be critical to utilize concrete-filled tubular sections in real construction works. This has prompted an experimental and numerical research program currently undertaken by the authors, aiming to investigate the behavior of concrete-filled tubular beam-column or column-to-column connections and devise design formulations for them, to facilitate the applications of concrete-filled tubular sections in practice.

In this study, the authors propose a novel RCFST column-to-column connection, where high strength steel rebars were set through the column, rather than employing full penetration welding, as shown in Fig. 2. Compared with the common column-to-column connection, the proposed innovative RCFST column-to-column connection possesses superior advantages in workability, construction convenience, and assumed to be well suited to the ultrahigh strength steel structures that are difficult to weld.

The current work is an attempt to study the flexural behavior of the novel RCFST column-to-column connection under monotonic loading. Four one-half scale column-to-column connections were tested under four-point bending to evaluate the flexural performance of the proposed RCFST column-to-column connection. Besides, the strain distribution of steel bars and steel tube is discussed in detail. This work aims to provide experimental results to evaluate the proposed new RCFST column-to-column connection and develop design formulae for calculating their bending resistances.

2. Experimental program

2.1 Test specimens

Four tested specimens were evaluated to investigate the flexural behavior of the new RCFST column-to-column connection manufactured by high strength steel under four-point bending. The scale factor was one half due to the limitation of the loading capacity of the testing apparatus. The key experimental parameter considered in the current study are column shape (square and circular) and the configuration of reinforcing steel bars (separated type and gathered type), as presented in Fig. 3 and Fig.4. The design process of square and circular connections is shown as follows. The section size of RCFST column is preliminarily selected by the Eq. (1) [27],

$$A = \frac{N_u}{0.9\varphi\left(\sigma_{cB} + \sigma'_{sy} \cdot \rho'\right)} \tag{1}$$

where, N_u is the designed bearing capacity of column under axial compression; φ is the stability coefficient of reinforced concrete (RC) members under axial compression; σ_{cB} is the compressive strength of concrete; σ'_{sy} is the compressive yield strength of reinforcing bar; ρ' is the economic reinforcement ratio obtained from engineering experience, taking 1.5%-2.0%.

According to Eq. (1), the cross-section of square column is selected as 300×300 mm, and the diameter of circular column is equal to 318.5 mm. Due to the separation between the upper and lower steel tubular of the connection, the contribution of steel tubes to the shear capacity of the column is deemed negligible. The cross-section area of the compression (A'_s) and tensile reinforcement (A_s) can be obtained by Equation (2a) and Equation (2b), respectively [27].

$$A'_s = \frac{M - \xi_b\left(1 - 0.5\xi_b\right) b h_0^2 \alpha_1 \sigma_{cB}}{\sigma'_{sy}\left(h_0 - a'_s\right)} \tag{2a}$$

$$A_s = \frac{\alpha_1 \sigma_{cB} b \xi_b h_0 + \sigma'_{sy} A'_s}{\sigma_{sy}} \tag{2b}$$

The total cross-section area of the reinforcement (A_0) in the circular specimen can be calculated by Equation (4), with the bars evenly distributed along the perimeter.

$$A_0 = \frac{\dfrac{N}{0.9\varphi} - \sigma_{cB} \cdot \pi r_0^2}{\sigma'_{sy}} \tag{3}$$

where M is the design bending resistance of the column section; ξ_b is the height of the relative compression zone; b is the side length of square section; h_0 is the effective height of section; a'_s is the distance from resultant point of the compressed steel bars to the edge of the section compression zone, as shown in Fig. 5(a); σ_{sy} is the tensile yield strength of steel bar, which is equal to the compressive yield strength (σ'_{sy}).

The compression zone and the tension zone need to be equipped with 10ϕ20 USD685 reinforcing bars. The thickness of steel tube (t) can be determined based on the design principle that the flexural bearing capacity of concrete filled steel tube is equal to that of reinforced concrete. The ultimate bending moment of reinforced concrete section of square and circular RCFST column (${}_sM_u$ and ${}_cM_u$) are calculated by Eq. (4) and Eq. (5) [28], respectively. The plastic ultimate bending moment of concrete filled steel tube (M_p) consists of two parts: compression zone and tension zone. The ultimate bending moment of compression zone (${}_sM_c$ and ${}_cM_c$) are calculated by Eq. (6) ~ Eq. (9) [28], and the ultimate bending moment of tension zone (${}_sM_s$ and ${}_cM_s$) are calculated by Eq. (10) ~ Eq. (12) [28]. Note that the tensile strength of the concrete is ignored in the calculation. The stress distribution diagram across the examined CFST sections is shown in Fig. 5.

$$M_u = \alpha_s \alpha_1 \sigma_{cB} b h_0^2 + \sigma'_{sy} A'_s \left(h_0 - a'_s\right) \tag{4}$$

$$\begin{cases} {}_cM_u = \dfrac{2}{3}\alpha_1 \sigma_{cB} r_0^3 \sin^3\theta + \sigma_{sy} A_s r_s \left(\dfrac{\sin\theta + \sin\pi\alpha_t}{\pi}\right) \\ {}_cN_0 = \alpha_1 \sigma_{cB} r_0^2 \left(\theta - \sin\theta\cos\theta\right) + \sigma_{sy} A_s \left(\dfrac{\theta}{\pi} - \alpha_t\right) = 0 \\ \alpha_t = 1.25 - \dfrac{2\theta}{\pi} \end{cases} \tag{5}$$

$$\begin{cases} {}_sx_c = \dfrac{b}{4} + \dfrac{x}{2} \\ {}_cx_c = \dfrac{2r_0\sin^3\theta}{3\left(\theta - \sin\theta\cos\theta\right)} \end{cases} \tag{6}$$

$$\begin{cases} {}_sA_c = b\left(\dfrac{b}{2} - x\right) \\ {}_cA_c = r_0^2\left(\theta - \sin\theta\cos\theta\right) \end{cases} \tag{7}$$

$$\begin{cases} {}_sM_c = {}_sA_c\sigma_{sc}^{y} \cdot {}_sx_c \\ {}_cM_c = {}_cA_c\sigma_{sc}^{y} \cdot {}_cx_c \end{cases} \tag{8}$$

$$\begin{cases} \sigma_{sc}^{y} = \left(1.212 + B\xi + C\xi^{2}\right)\sigma_{cB} \\ B = 0.1759\dfrac{\sigma_{sy}}{235} + 0.974 \\ C = -0.1038\dfrac{\sigma_{cB}}{20} + 0.0309 \\ \xi = \dfrac{\alpha\sigma_{sy}}{\sigma_{cB}} \end{cases} \tag{9}$$

$$\begin{cases} {}_sx_s = \dfrac{b}{4} - \dfrac{x}{2} \\ {}_cx_s = r_0\dfrac{\sin\theta}{\theta} \end{cases} \tag{10}$$

$$\begin{cases} {}_sA_t = 2\left(b + x\right)t \\ {}_cA_t = 2r_0\left(\pi - \theta\right)t \end{cases} \tag{11}$$

$$\begin{cases} {}_sA_t = 2\left(b + x\right)t \\ {}_cA_t = 2r_0\left(\pi - \theta\right)t \end{cases} \tag{12}$$

Where, ${}_sA_c$ and ${}_cA_c$ are the section area of compression zone of square and circular column; $\sigma^{y}{}_{sc}$ is the yield strength of axial compression composite materials; r_0 is the radius of circular concrete section; r_s is the circumferential radius of rebar's barycenter; θ is the semi-central angle of neutral axis; α_t is the area ratio of tensile bars to all bars; ${}_sx_c$ and ${}_cx_c$ are the barycenter coordinates of the compression zone; x is the shortest distance from the center of cross-section to the edge of concrete compression zone; ξ is the hoop coefficient; ${}_sA_t$ and ${}_cA_t$ are the section area of steel tube in the tension zone; ${}_sx_s$ and ${}_cx_s$ are the barycenter coordinates of the tension zone. At the limit state of the concrete filled steel tube, the tension force is equal to the compression force, as shown in Eq. (13).

Based on the equilibrium in Eq. (14), the thickness of steel tube (t) is therefore calculated to be equal to 6 mm, which was adopted as the nominal thickness in the experimental program.

$$A_c \sigma_{sc}^{y} = A_t \sigma_{sy} \tag{13}$$

$$M_u = M_p \tag{14}$$

The studied square or circular column-to-column connections comprised of square hollow section (SHS) with the nominal cross-section dimensions of 300×300×6.0 mm (outer width × outer depth × wall thickness) and circular hollow section (CHS) with nominal cross-section dimensions of 318.5×6.0 mm (outer diameter × wall thickness), which were fabricated from high strength steel sheets with a grade of H-SA700 using thermomechanical control technology [29]. The reinforcing bars were made of high strength steel with grade USD 685, with a nominal yield stress of 685 MPa, following the manufacturing process setout in Japanese Industrial Standards [30]. RCFST column-to-column connection specimens comprised of two identical RCFST columns with the infilled concrete and reinforcing bars continued in the connections, while leaving a gap of 10 mm between the outer steel tubes. After pouring concrete inside the steel tubes, the gap between steel tubes was filled with filling mortar. The steel bars in steel tubes were fixed by upper and lower steel bar restraint plates whose four corners were welded with steel tubes. Four steel plates were welded in the internal surfaces of the steel tubes to improve the mechanical interaction between the steel tubes and the concrete infill, as well as enhance the bond-slip strength of the column connections. The total lengths of the test specimens were 2010 mm, and the reinforcing steel bars had a nominal length of 2000 mm, offsetting 5 mm from each end of the specimen. A summary of the key parameters of the four test specimens is reported in Table 1. The identifier of each column specimen is composed of the cross-sectional shape and the reinforcement configuration type, with‘S’ or ‘C’ representing the section shape of the square or circular column and followed by ‘S’ or ‘G’ =corresponds to the configuration of reinforcing steel bars being separated or gathered, respectively.

Table 1 Properties of specimens

2.2 Material properties of steel and concrete

Based on JIS Z2241 [31], the material properties of steel column and reinforcing bars were obtained from tensile coupon tests. The tensile coupon specimens were tested in a 200-ton testing machine with a consistent speed of 0.3 mm/min [32]. The material properties of H-SA700 and USD 685 are shown in Table 2.

Table 2 Material properties of steel tubes and reinforcing bars.

The 28-day compressive strengths were obtained from cylinder tests following JIS A1108 [33]. The specimens were tested when column-to-column connection tests were conducted (35, 40, 45, and 47 days after casting). The peak strain corresponding to the ultimate strength on the concrete compressive stress-strain curve is the concrete compressive strain. The compressive strain (ε_c), compressive strength (σ_{cB}), and Young’s modulus (E_c) are shown in Table 3.

Table 3 Material properties of concrete

2.3 Test setup and measurements

Fig. 6 shows the test setup of a RCFST column-to-column specimen. A 5000 kN capacity compression testing machine was used to apply the vertical loading at the top surface of the loading girder, which was connected to two solid steel cylinders in the bottom surface to transfer loadings from the compression machine to the tested column-to-column connection. Teflon plates were used to reduce friction that may exist if the horizontal deformations of the test specimen occurred in the transfer system. Sliding rollers were set on the bottom of the column-to-column connection to provide roller supports that allow horizontal displacements.

Fig. 7 shows the instrumentation of LVDTs on the column-to-column connection. The flexure deformation of column-to-column connection is measured by fourteen LVDTs, which are set on both sides of the specimen, as shown in Fig.7. On each side, two vertical LVDTs are symmetrically arranged at 25mm, 325mm, and 550mm away from the center lines of the joint, respectively, to obtain the vertical displacement of each measuring point under bending. A horizontal LVDT is installed at the welded steel plate on the upper and lower sides of the joint to measure and calculate the horizontal relative displacement between the compression zone and the tension zone of the specimen. Strain gauges were also used to record the strain development histories near the middle sections, the configuration of the strain gauges on the steel tube and rebars are illustrated in Fig. 8. The uniaxial strain gauges on the tension and compression reinforcing bars are respectively pasted on the centerline of the joint, and 190mm and 300mm away from the centerline. Steel plates are welded up and down at the connection, resulting in the biaxial strain gauge between the ribs deviating from the central axis of the steel tube, while the other two biaxial strain gauges are affixed to the 185mm and 300mm away from joint on the centerline of the steel tube tension zone and compression zone, respectively. As a result, the strain distributions on the reinforcing bars and steel tubes around the column connections are measured.

The flexure deformation angle (θ,θ_j) of specimen and connection, as shown in Fig. 9, are defined by Eq. (15) and Eq. (16),

$$\theta_j = \frac{\delta_1 - \delta_2}{2d}, \quad \theta = \frac{\delta_3 - \delta_5}{l} \qquad (15), (16)$$

where, δ_1 is the horizontal displacement on the top of the specimen; δ_2 is the horizontal displacement on the bottom of the specimen; δ_3, δ_4, and δ_5 are the vertical displacements offset from the middle of the specimen by 25 mm, 325 mm, and 550 mm, respectively; The displacement value is assumed to be positive in shrinkage and negative in the stretch.

2.4 Definition of key performance points

The stiffness (K), yield bending moment point (M_y, θ_y), and plastic bending moment point (M_p, θ_p) are defined according to the skeleton curves [34,35], as shown in Fig. 10.

3. Experimental Results

3.1 Failure mode of column-to-column connection

Fig. 11 shows the failure photographs of all the column-to-column connections. The deformations of all the tested specimens were found to be symmetric. The crack of concrete mainly distributed in the tensile region of the connection parts, while concrete was observed to crush in the compress region. The crack of the infilled concrete was initiated and propagated at the connection parts. The maximum crack width was measured to be approximately 20 mm at the drift angle θ= 0.05 rad, as shown in Fig. 11 (b.iv).

Fig. 11(a.i) shows the overall failure phenomenon of Specimen S-S. Concrete cracks occurred at the column-column connection at θ=0.008 rad. The specimen S-S reached the yield point at θ=0.011 rad and entered the plastic stage at θ=0.014 rad. The specimen showed a significant bending deformation. The concrete around the column-column connection suffered from a brittle fracture in tension at θ=0.058 rad (Fig. 11(a.ii)) and crushing in compression (Fig. 11(a.iii)). The maximum crack reached 17 mm in tension (Fig. 11(a.iv)).

Fig. 11(b.i) shows the overall failure phenomenon of Specimen S-G. Concrete cracks appeared at the column-column connection at θ=0.009 rad. The specimen S-G entered the yield stage at θ = 0.011 rad and reached the plastic point at θ=0.014 rad. Similar to the Specimen S-S, the Specimen S-G also manifested an obvious bending deformation. The concrete around the column-column connection occurred brittle failure in tension (Fig. 11(b.ii)) and crushing in compression (Fig. 11(b.iii)) at θ=0.065 rad. The maximum crack reached 22 mm in tension (Fig. 11(b.iv)).

Fig. 11(c.i) shows the overall failure phenomenon of Specimen C-S. Concrete cracks appeared at the column-column connection at θ=0.007 rad. The Specimen C-S entered the yield stage at θ=0.009 rad and reached the plastic point at θ=0.01 rad. Different from the square specimens, the Specimen C-S appeared limited bending deformation. The concrete around the column-column connection occurred brittle failure in tension (Fig. 11(c.ii)) and crushing in compression (Fig. 11(c.iii)) at θ=0.041 rad. The maximum crack reached 15 mm in tension (Fig. 11(c.iv)).

Fig. 11(d.i) shows the overall failure phenomenon of specimen C-G. Concrete cracks appeared at the column-column connection at θ=0.007 rad. The Specimen C-G entered the yield stage at θ = 0.009 rad and reached the plastic point at θ=0.013 rad. The Specimen C-G showed a slight bending deformation. The concrete around the column-column connection occurred brittle failure in tension (Fig. 11(d.ii)) and crushing in compression (Fig. 11(d.iii)) at θ=0.038 rad. The maximum crack reached 13 mm in tension (Fig. 11(d.iv)).

3.2 Bending moment to drift angle relationship

All the column-to-column connections exhibited outstanding deformation capabilities. The monotonic bending moment to drift angle curves M–θ or M–θ_j are plotted in Fig. 12, where a linear relationship was observed with the drift angle reaching approximately 0.01 rad, followed by pronounced plastic deformation. Table 4 summarises the key structural performance parameters of the column-to-column connections. It was found that with the increase of the drift angle, the θ_j/θ of the four specimens stabilized and finally converged at approximately 0.90, as shown in Fig. 12(c). The minimal differences between M-θ and M-θ_j indicated that the deformations of the tested specimens mainly concentrated at the middle part of the connections, rather than the adjacent columns.

The influence of the arrangement of the reinforcing steel bars on the structural performance of the investigated CFST connections was examined through comparisons of the bending moment–drift angle curves for the test specimens S-S and S-G in Fig. 12(a), where it is apparent that the separated configuration of the reinforcing steel bars in connections significantly enhanced the ultimate performance of the connections with square outer tubes; the M_y and M_p of specimen S-G increased by 25.0% and 26.8%, respectively compared to their counterparts of specimen S-S. However, the configuration of reinforcing steel bars in connections with circular outer tubes seemed to be less influential compared to those in connections with square outer tubes, as can be seen from Fig. 12(b) that the curves obtained from No. 3 specimen with separated embedded reinforcing bars remained almost unaltered from those obtained from No. 4 specimen with gathered reinforcing bars. Compared with specimen C-S, the M_y and M_p of specimen S-G increased by 3.0% and 10.0%, respectively. Overall, it can be seen that the configuration of reinforcing steel bars has a great influence on the ultimate performance of column-to-column specimens. In order to further quantify the influence of the outer tube and the reinforcing bars, analysis of strain distribution was carried out based on the readings recorded from the strain gauges in the experiments and reported in the following sections.

4. Strain distribution of steel bars and steel tube

The cross-sectional layout of the strain gauges attached to steel reinforcing bars in the middle parts of the connections is presented in Fig. 13(a). Additionally, two pairs of strain gauges were arranged in the adjacent column part, offsetting a distance of 190 mm and 300 mm from the centerline of a tested specimen, as shown in Fig. 13(b). The distribution of the strain gauges attached to steel outer tubes of the connections is presented in Fig. 14, where the strain rosettes were mounted on both sides symmetrically: S1 to S4 located in the middle line of the two ribbed stiffeners, 85 mm from the connection part; S5 to S8 located on the middle line of the column, offsetting 185 mm from the connection seam; S9 to S12 located on the middle line of the column, offsetting 300 mm from the connection part. The odd number rosettes were used to make a record of the strain development in the axial longitudinal direction, while the even number rosettes measured the development of the hoop strain.

4.1 Strain distribution of steel bar around the connection part

Fig. 15 shows the strain of steel bars of all specimens around the connection part. The vertical axis represents the strain of the steel bar and the horizontal axis represents the drift angle. The yield strain of the steel bar was 0.0036, which was also obtained by the coupon test of the material. The outermost steel bars located far away from the centroid of the column started to yield at θ = 0.01 rad. Other steel bars yield at θ = 0.01 rad, except the innermost steel bars. Column shape and configuration of reinforcing steel bars has little effect on the strain distribution of steel bars.

4.2 Strain distribution of steel bar far away from the connection part

Fig. 16 shows the strain of steel bars of all specimens far away from the connection part. All the steel bars stayed in the elastic stage during the whole test. It is obvious that with the increase in distance from the seam, the strain of steel bar decrease.

4.3. Strain distribution of steel tube

Fig. 17 shows the strain of the steel tube of all specimens. The vertical axis represents the strain of the steel tube and the horizontal axis represents the drift angle. The yield strain was 0.0037 for the square tube and 0.0038 for the circular tube, which was obtained by the coupon test. During the whole testing, all the steel tube stayed in the elastic stage. The minimum axial strain occurred on S1 in the compress region. In addition, the maximum hoop strain occurred on S2 in the tensile region. Although the configuration of reinforcing steel bars was different, the strain distribution of steel tube, with the same column type, showed a similar tendency.

As for square specimen (S-S and S-G), the minimum axial strain occurred on the S1 and S3. With the increase of distance from the connection part, the axial strain increased gradually. The axial strain of S3 was the smallest one in the tensile region. It indicated that the tensile stress in the steel tube was transferred by the rib stiffener. The hoop strain of S6 and S10 has a large difference in the compressive region. One of the reasons is that the infilled concrete expanded, resulting in the expansion of the steel tubes. The maximum hoop strain occurred on the S2 and S4. With the increase of distance from the connection part, the hoop strain decreased gradually. The axial strain of S2 was the biggest one in the compressive region. The circular specimens (C-S and C-G) have a similar tendency, as shown in Fig. 17.

5. Calculation method

5.1 Yield strength of RCFST column

According to the AIJ Standard for Structural Calculation of Reinforced Concrete Structures [36], the yield strength of RCFST column is calculated supposing that:

(1) All the materials conform to the plane section assumption.

(2) The constitutive relationship of concrete is linear during the elastic stage, as shown in Fig. 18(a) and Eq. (17). The short-term allowable stress remains constant when it reaches to the short-term allowable stress (f_{cs}). The short-term allowable strength of concrete is twice of long-term strength, which is 1/3 of concrete compressive strength (σ_{cB}) [37,38]. In addition, concrete does not bear tensile stress.

$$\sigma_c = \begin{cases} E_{cs} \cdot \varepsilon_c \left(0 \le \varepsilon_c < \varepsilon_{cs}\right) \\ f_{cs}\left(\varepsilon_{cs} \le \varepsilon_c\right) \end{cases}, \; f_{cs} = \frac{2}{3}\sigma_{cB} \tag{17}$$

(3) The stress-strain relationship of steel is linear until it gets to the yield stress (f_{sy}), as shown in Fig. 18(b) and Eq. (18). Moreover, the stress-strain relationship of steel is symmetric in compression and tension.

$$\sigma_s = \begin{cases} f_{sy}\left(\varepsilon_{sy} \le \varepsilon_s\right) \\ E_s \cdot \varepsilon_s \left(-\varepsilon_{sy} < \varepsilon_s < \varepsilon_{sy}\right) \\ -f_{sy}\left(\varepsilon_s \le -\varepsilon_{sy}\right) \end{cases}, \; f_{sy} = \sigma_{sy} \tag{18}$$

Where, σ_{cB} is the compressive strength of concrete; ε_{cs} is concrete strain corresponding to short-term allowable stress (f_{cs}) in the coupon test; E_{cs} is the ratio of short-term allowable stress (f_{cs}) to strain (ε_{cs}); σ_{sy} and ε_{sy} are the yield stress and strain of steel bar obtained from coupon test, respectively; E_s is Young's modulus of steel bar obtained from coupon test [39-42].

(4) The distribution of yielding steel bars is shown in the red part of Fig. 19. The steel bars at the outermost edge of the square RCFST reached yield point first, while the circular ones yielded at an angle of ±45° to the vertical symmetrical axis of the section. The stresses on the same row are concentrated at one point while calculating the yield stress of rebars.

Where, D_c is the diameter of infilled square concrete; d_j is the distance from the edge of compression side to the steel bars in row j; x_n is the distance from the outermost edge of compression side to the neutral axis; σ_{sj} and ε_{sj} are the stress and strain of steel bars in row j; $\sigma_{c\max}$ and $\varepsilon_{c\max}$ are the maximum stress and strain of concrete in the strain distribution diagram.

The yield strength is obtained by directly superimposing the contribution of high strength steel bars and infilled concrete. Fig. 20 illustrates the stress-strain distribution when the connections reach to yield point. According to the position of the neutral axis and the strain of concrete, the section stress distribution at different stages is determined. The triangle and rectangular stress distributions of concrete are defined as region 1 and region 2, respectively.

The yield strength (N_y and M_y) are obtained by Eq. (19). The steel parts (N_s and M_s) are calculated by Eq. (20). The concrete parts (N_c and M_c) are calculated by Eq. (21) and Eq. (22). In addition, the internal force of regions 1 and 2 in the square RCFST is calculated by Eq. (23) and Eq. (24), while the circular ones are calculated by Eq. (25) and Eq. (26).

$$\begin{cases} N_y = N_c + N_s (= 0) \\ M_y = M_c + M_s \end{cases} \tag{19}$$

$$\begin{cases} N_s = \sum \sigma_{sj} \cdot a_j \\ M_s = \sum \sigma_{sj} \cdot a_j \cdot \left(\dfrac{D_c}{2} - d_j \right) \end{cases} \tag{20}$$

$$N_c = \begin{cases} N_{c1} (0 \le \varepsilon_{c\max} \le \varepsilon_{cs}) \\ N_{c1} + N_{c2} (\varepsilon_{cs} < \varepsilon_{c\max}) \end{cases}, \quad M_c = \begin{cases} M_{c1} (0 \le \varepsilon_{c\max} \le \varepsilon_{cs}) \\ M_{c1} + M_{c2} (\varepsilon_{cs} < \varepsilon_{c\max}) \end{cases} \qquad (21), (22)$$

$$\begin{cases} N_{c1} = \dfrac{1}{2}\sigma_{c1}x_1 D_c \\ M_{c1} = \dfrac{1}{2}\sigma_{c1}x_1 D_c \cdot x_{g1} \end{cases}, \begin{cases} N_{c2} = f_{cs}(x_n - x_1)D_c \\ M_{c2} = f_{cs}(x_n - x_1)D_c \cdot x_{g2} \end{cases} \tag{23), (24}$$

$$\begin{cases} N_{c1} = \dfrac{D_c^2 \cdot \sigma_{c1}}{4x_1}\left[\dfrac{D_c}{3}\sin^3\theta_x - \dfrac{D_c - 2x_n}{4}\left(2\theta_x - \sin 2\theta_x\right)\right]_{\theta_1}^{\theta_n} \\ M_{c1} = \dfrac{D_c^3 \cdot \sigma_{c1}}{8x_1}\left[\dfrac{D_c}{8}\left(\theta_x - \dfrac{1}{4}\sin 4\theta_x\right) - \dfrac{D_c - 2x_n}{3}\sin^3\theta_x\right]_{\theta_1}^{\theta_n} \end{cases} \tag{25}$$

$$\begin{cases} N_{c2} = \dfrac{1}{8}D_c^2 \cdot f_{cs}(2\theta_1 - \sin 2\theta_1) \\ M_{c2} = \dfrac{1}{12}D_c^3 \cdot f_{cs}\sin^3\theta_1 \end{cases} \tag{26}$$

Where, a_j is the total section area of rebars in row j; σ_{c1} is the maximum stress in region 1; x_1 is the distance from the neutral axis to the boundary of region 1; x_{g1} and x_{g2} are the distances from the center of cross section to the acting points of resultant forces N_1 and N_2, respectively. θ_1 and θ_n are the semicircular center angle corresponding to regions 1 and 2, respectively.

5.2 Calculation of ultimate strength

Supposing that the whole cross-section plane is plasticity when it reaches to the ultimate stage, as shown in Fig. 21. The calculation method of ultimate strength is similar to that of yield strength. The ultimate strength (N_u and M_u) are obtained by Eq. (27). The ultimate strength of steel bars (N_{su} and M_{su}) are calculated by Eq. (28). The ultimate strength of concrete (N_{cu} and M_{cu}) in square and circular RCFST are respectively calculated by Eq. (29) and Eq. (30).

$$\begin{cases} N_u = N_{cu} + N_{su}\left(=0\right) \\ M_u = M_{cu} + M_{su} \end{cases} \tag{27}$$

$$\begin{cases} N_{su} = \sum a_j \cdot \sigma_{syj} \\ M_{su} = \sum a_j \cdot \sigma_{syj} \left(\dfrac{D_c}{2} - d_j \right) \end{cases} \tag{28}$$

$$\begin{cases} N_{cu} = x_n \cdot D_c \cdot \sigma_{cB} \\ M_{cu} = \dfrac{1}{2}\left(D_c - x_n\right) x_n \cdot D_c \cdot \sigma_{cB} \end{cases}, \quad \begin{cases} N_{cu} = \left(\theta_n - \sin\theta_n \cdot \cos\theta_n\right) \dfrac{D_c^2 \cdot \sigma_{cB}}{4} \\ M_{cu} = \sin^3\theta_n \dfrac{D_c^3 \cdot \sigma_{cB}}{12} \end{cases} \qquad (29), (30)$$

5.3 Comparison between experimental and calculated results

Fig.22 shows the moment-angle curves compared with the experimental and calculated results. The red and blue lines represent the yield and ultimate strength obtained by calculation formula, respectively. In addition, the red triangle point and blue circular point represent the yield and ultimate strength obtained by experiments. It is obvious that the calculation formulae underestimate the yield strength of tested specimens and overestimate the ultimate strength of tested specimens. The main reason is that the stress of concrete does not reach the allowable strength when the specimens reached the yield point. Moreover, there isn’t any steel bar to get to the plastic stage when the specimens reached the ultimate point in tests.

Table 5 lists the comparisons between the experimental and calculated results in detail. The yield strength and plastic strength are 104% ~116% and 85%~91% of the tested results. Although the calculated formulae match with the tested results, the finite element analysis will be conducted to verify the reliability in the following paper.

6. Conclusions

This paper has reported an experimental investigation into the flexural behavior of a novel high strength steel column-to-column connection. A total of four combinations of connections outer tube shape and configuration of reinforcing bars were considered. The outer tubes employed alternative SHS or CHS, while the configuration of the reinforcing bars was either gathered or separated type. The following conclusions have been obtained:

(1) The gathered type of reinforcing steel bars can significantly improve the flexural capacities of the proposed connections with square outer tubes. However, the influence of the configuration of the reinforcing steel bars on the ultimate performance of connections with circular outer tubes was insignificant. Analyses of strain distribution indicated that the configuration of the reinforcing steel bars had minimal effects on either the strain distribution of steel tube or steel bars and as well we the failure modes of the connections.

(2) Although the column shape had little influence on the strain distribution of steel bars and failure modes, it dramatically altered the strain distribution of the steel tubes.

(3) The proposed formulae agree with the experimental results of the yield and ultimate strength, although the calculated formulae underestimate the yield strength and overestimate the ultimate strength.

Acknowledgments

Mou Ben was financially supported by the iSMART (201812003) and Natural Science Funding of Shandong Province (ZR2020EEB38). In addition, Professor Akihiko Kawano, Professor Shintaro Matsuo from Kyushu University, Professor Wei Pan from University of Hong Kong, and Mr. Yong Zhao from Southeast University, are greatly appreciated for their valuable help and advice on this study.

References

[1] Shanmugam N E, Lakshmi B. State of the art report on steel-concrete composite columns[J]. Journal of constructional steel research, 2001, 57(10): 1041-1080.

[2] Mou B., Bai Y., Experimental investigation on shear behavior of H-shaped beam-to-CFST column

connections with irregular panel zone[J]. Engineering Structures, 2018, 168(08):487-504.

[3] F. Wang, B. Young, L. Gardner, Experimental Study of Square and Rectangular CFDST Sections with Stainless Steel Outer Tubes under Axial Compression[J]. Journal of Structural Engineering, 2019, 145(11):04019139.

[4] Qiao Q, Zhang W, Mou B, et al. Seismic behavior of exposed concrete filled steel tube column bases with embedded reinforcing bars: Experimental investigation[J]. Thin-Walled Structures, 2019, 136: 367-381.

[5] Chen B C, Wang T L. Overview of concrete filled steel tube arch bridges in China[J]. Practice periodical on structural design and construction, 2009, 14(2): 70-80.

[6] Kang J Y, Choi E S, Chin W J, et al. Flexural behavior of concrete-filled steel tube members and its application[J]. International Journal of Steel Structures, 2007, 7(4): 319-324.

[7] Han L H, An Y F. Performance of concrete-encased CFST stub columns under axial compression[J]. Journal of Constructional Steel Research, 2014, 93: 62-76.

[8] Wang X, Liu J, Zhang S. Behavior of short circular tubed-reinforced-concrete columns subjected to eccentric compression[J]. Engineering Structures, 2015, 105: 77-86.

[9] Jiang A, Chen J, Jin W. Experimental investigation and design of thin-walled concrete-filled steel tubes subject to bending[J]. Thin-Walled Structures, 2013, 63: 44-50.

[10] Chitawadagi M V, Narasimhan M C. Strength deformation behaviour of circular concrete filled steel tubes subjected to pure bending[J]. Journal of Constructional Steel Research, 2009, 65(8-9): 1836-1845.

[11] Wang R, Han L H, Nie J G, et al. Flexural performance of rectangular CFST members[J]. Thin-Walled Structures, 2014, 79: 154-165.

[12] Tao Z, Song T, Uy B, et al. Bond behavior in concrete-filled steel tubes[J]. Journal of Constructional

Steel Research, 2016: 81-93.

[13] Dong H, Chen X, Cao W, et al. Bond behavior of high-strength recycled aggregate concrete-filled large square steel tubes with different connectors[J]. Engineering Structures, 2020.

[14] Dong H, Chen X, Cao W, et al. Bond-slip behavior of large high-strength concrete-filled circular steel tubes with different constructions[J]. Journal of Constructional Steel Research, 2020.

[15] Alatshan F, Osman S A, Hamid R, et al. Stiffened concrete-filled steel tubes: A systematic review[J]. Thin-walled Structures, 2020.

[16] Lee C, Chang K. Numerical Investigation on the Behavior of Circumferentially Butt-Welded Steel Circular Hollow Section Flexural Members[J]. Journal of Structural Engineering, ASCE, 2011, 137(12): 1395-1404.

[17] Wang Y Q, Zong L, Shi Y J, et al. Bending behavior and design model of bolted flange-plate connection[J]. Journal of Constructional Steel Research, 2013, 84(84): 1-16.

[18] Liu X, He X N, Wang H, et al. Compression-bend-shearing performance of column-to-column bolted-flange connections in prefabricated multi-high-rise steel structures[J]. Engineering Structures, 2018: 439-460.

[19] Haaijer G. Economy of high strength steel structural members[J]. Journal of the Structural Division, 1961, 87(8): 1-24.

[20] Van Long H, Jean-François D, Lam L D P, et al. Field of application of high strength steel circular tubes for steel and composite columns from an economic point of view. Journal of Constructional Steel Research, 2011, 67(6): 1001-1021.

[21] Gho W M, Liu D. Flexural behaviour of high-strength rectangular concrete-filled steel hollow sections. Journal of Constructional Steel Research, 2004, 60(11): 1681-1696.

[22] Wang F, Young B, Gardner L. Compressive testing and numerical modelling of concrete-filled double skin CHS with austenitic stainless steel outer tubes. Thin-Walled Structures. 2019;141:345-59.

[23] Li G, Liu D, Yang Z, et al. Flexural behavior of high strength concrete filled high strength square steel tube[J]. Journal of Constructional Steel Research, 2017, 128: 732-744.

[24] Choi I R, Chung K S, Kim C S. Experimental study on rectangular CFT columns with different steel grades and thicknesses[J]. Journal of Constructional Steel Research, 2017, 130: 109-119.

[25] Chang X, Wei Y Y, Yun Y C. Analysis of steel-reinforced concrete-filled-steel tubular (SRCFST) columns under cyclic loading. Construction and Building Materials, 2012, 28(1): 88-95.

[26] Hua W, Wang H J, Hasegawa A. Experimental study on reinforced concrete filled circular steel tubular columns. Steel and Composite Structures, 2014, 17(4): 517-533.

[27] GB 50010-2010, Code for design of concrete structures[S]. Beijing: China Architecture Industry Press, 2010. (In Chinese)

[28] GB 50936-2014, Technical code for concrete filled steel tubular structures[S]. Beijing: China Architecture Industry Press, 2014. (In Chinese)

[29] Nishioka K. Market Requirement of Thermomechanically Processed Steel for 21th Century[C]//Proc. of TMCP International Conference, London, 2000. 2000.

[30] JIS. G0201, Glossary of Terms used in Iron and Steel (Heat Treatment) [S], Japanese Industrial Standards Committee, Tokyo, 2000.

[31] JIS Z2241, Metallic materials – tensile testing – method of test at room temperature [s]. Tokyo: Japanese Industrial Standards Committee; 2011.

[32] Tension or compression testing machines--Verification and calibration of the force measuring system [S]. Japanese Industrial Standards Committee, Tokyo, 2009.

[33] JIS A1108, Method of test for compressive strength of concrete [S]. Japanese Industrial Standards Committee, Tokyo, 2006.

[34] Mou B, Li X, Qiao Q Y, et al. Seismic behavior of frame corner joints under bidirectional cyclic loading test[J]. Eng. Struct, 2019, 196: 109316.

[35] Mou B, Zhao F, Qiao Q, et al. Flexural behavior of beam to column joints with or without an overlying concrete slab[J]. Engineering Structures, 2019, 199: 109616.

[36] Architectural Institute of Japan (AIJ). AIJ Standard for Structural Calculation of Reinforced Concrete Structures [J]. 2010. (In Japanese)

[37] Ben Mou, Yongtao Bai, Vipul Patel, Post-local buckling failure of slender and over-design circular CFT columns with high-strength materials, Engineering Structures, 2020, 210 (05):110197

[38] Ben Mou, Xi Li, Yongtao Bai, V. I. Patel, Numerical evaluation on shear behavior of irregular steel beam-to-CFST column connections, Journal of construction steel research, 2018 , 148(09): 422-435.

[39] Z.Q. Jiang, X.F. Yang, C. Dou, C. Li, A.L. Zhang, Cyclic testing of replaceable damper: Earthquake-resilient prefabricated column-flange beam-column joint, Eng. Struct. 183 (2019) 922–936.

[40] Ben Mou, Liyi Pang, Qiyun Qiao, Yiting Yang, Experimental investigation on unequal-depth-beams to column joint with t-shape connector, Engineering Structures, Elsevier, 2018, 174(11):663-674.

[41] Ben Mou, Xi Li, Yongtao Bai, Lisa Wang, Shear Behavior of Panel Zones in Steel Beam-to-Column Connections with Unequal Depth of Outer Annular Stiffener, Journal of Structural Engineering, ASCE, 2019, 145(2): 04018247

[42] A.L. Zhang, H. Zhang, Z.Q. Jiang, C. Li, X.C. Liu, Low cycle reciprocating tests of earthquake-resilient prefabricated column-flange beam-column joints with different connection forms, J. Constr. Steel Res. 164 (2020), 105771.

Table 1 Properties of specimens

Specimens	Cross-section shape	Outer tube section [mm]	Configuration of reinforcing steel bars
S-S	Square	300×300×6.0	Separated type
S-G	Square	300×300×6.0	Gathered type
C-S	Circular	318.5×6.0	Separated type
C-G	Circular	318.5×6.0	Gathered type

Table 2 Material properties of steel tubes and reinforcing bars.

Part	Steel type	Thickness (Diameter) [mm]	Young's modulus [N/mm^2]	Yield stress [N/mm^2]	Tensile stress [N/mm^2]	Yield ratio [%]	Elongation [%]
Square column	H-SA700	6.3	206,000	762	822	92.7	19.7
Circular column	H-SA700	6.1	202,000	769	820	93.8	18.1
Implanted reinforced bar	USD685	19.5	193,000	722	906	79.7	13.8

Table 3 Material properties of concrete

Specimen	E_c [N/mm^2]	σ_{cB} [N/mm^2]	ε_c [%]
S-S	40,000	78.07	0.27
S-G	39,200	78.13	0.25
C-S	40,400	78.19	0.27
C-G	39,700	78.22	0.26

Table 4 Experimental stiffness and bending moment of specimens

Specimen	K_e [kN/rad]	M_y [kN·m]	θ_y [rad]	M_u [kN·m]	θ_u [rad]
S-S	39384	367.61	0.0108	392.06	0.0137
S-G	45706	459.69	0.0109	497.14	0.0144
C-S	45130	349.06	0.0089	365.04	0.0103
C-G	45229	359.36	0.0091	400.44	0.0130

Table 5 Comparison between experimental value and calculated value of strength

Specimen	M_y	M_{ye}	M_{ye}/M_y	M_u	M_{ue}	M_{ue}/M_u
S-S	320.0	367.8	1.15	451.0	399.5	0.89
S-G	441.2	460.2	1.04	577.2	489.3	0.85
C-S	308.8	349.0	1.13	397.3	361.2	0.91
C-G	315.5	365.6	1.16	447.1	387.3	0.87

Note: M_y and M_{ye} represent the calculated and experimental values of yield strength, while M_u and M_{ue} represent the calculated and experimental values of ultimate strength, respectively.

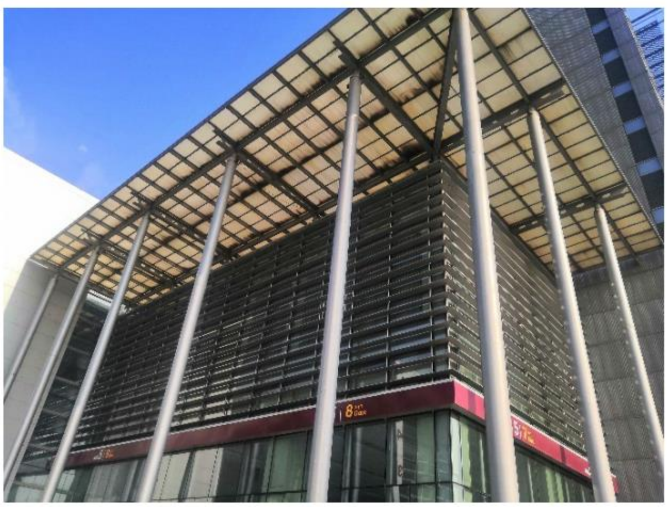

Fig. 1 The use of CFST columns in an exhibition hall

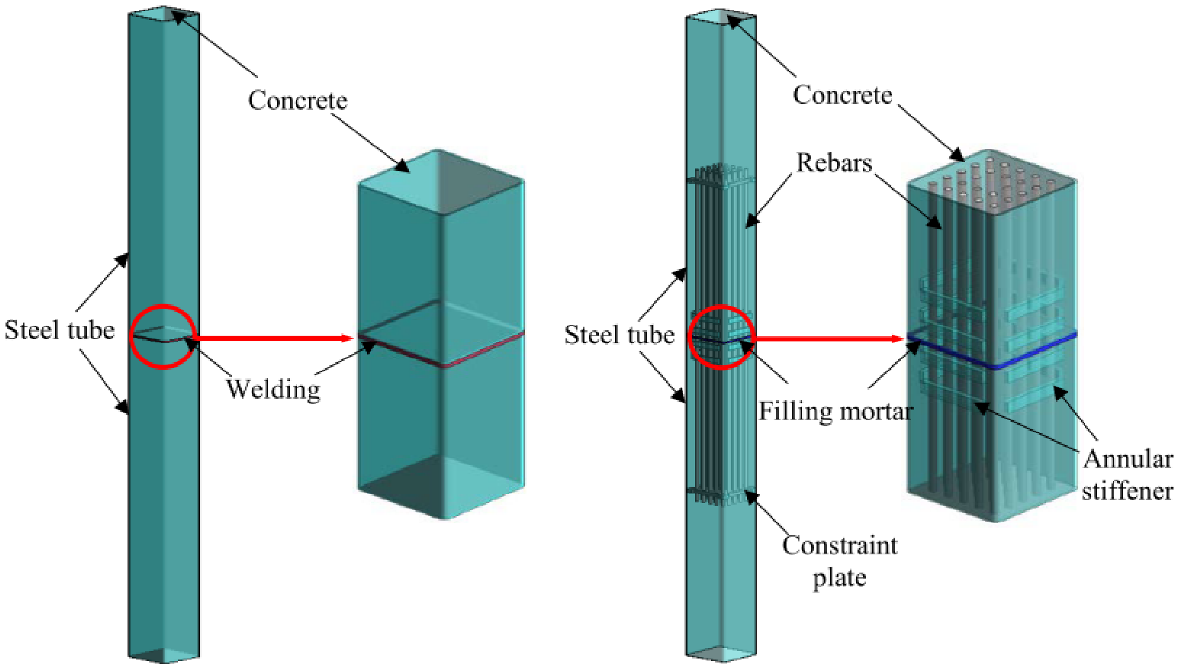

(a) Common column-to-column connection (b) Novel column-to-column connection

Fig. 2 Comparison diagram of RCFST column-to-column connections

524

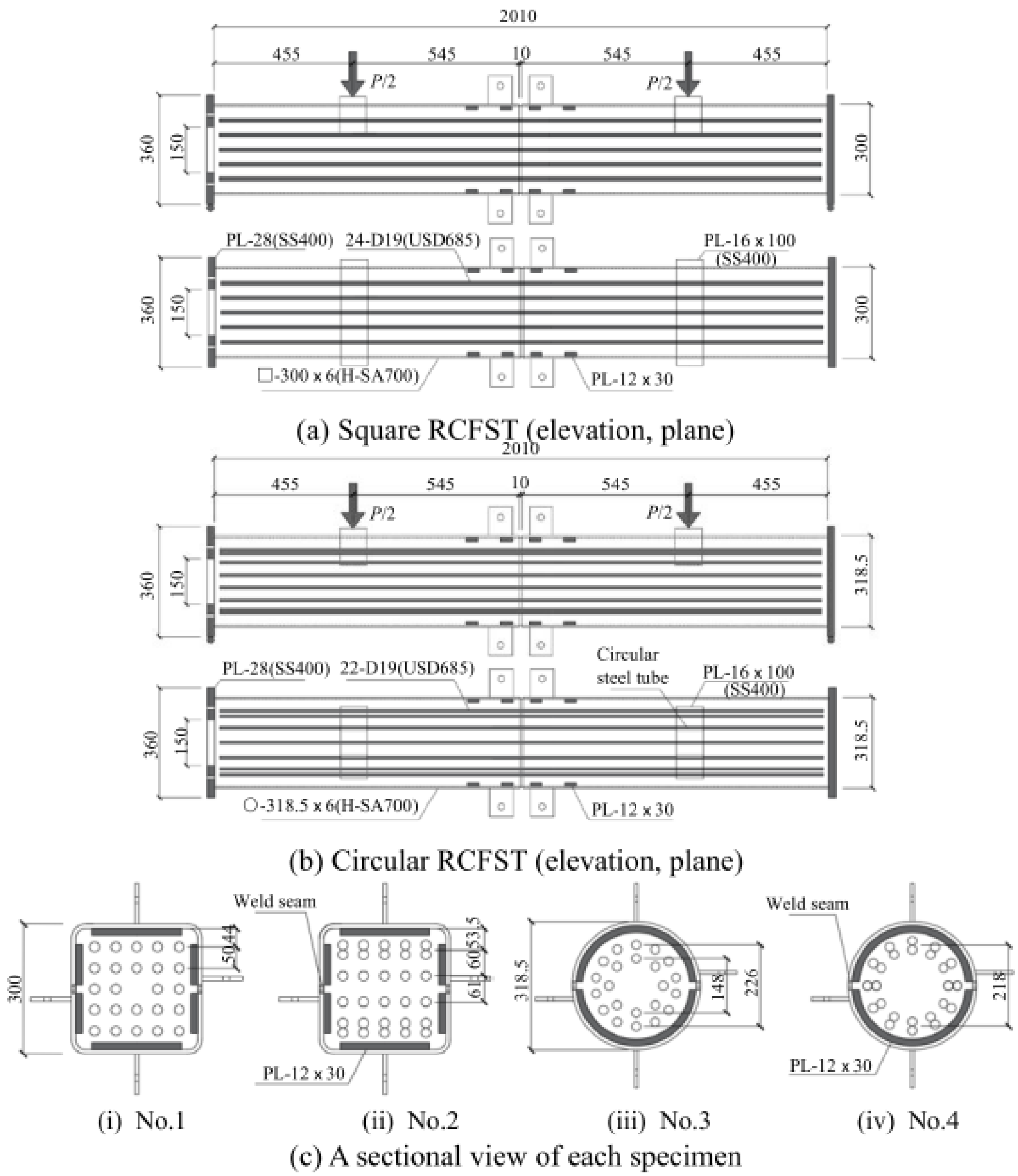

Fig. 3 Schematic diagrams of specimens (Unit: mm)

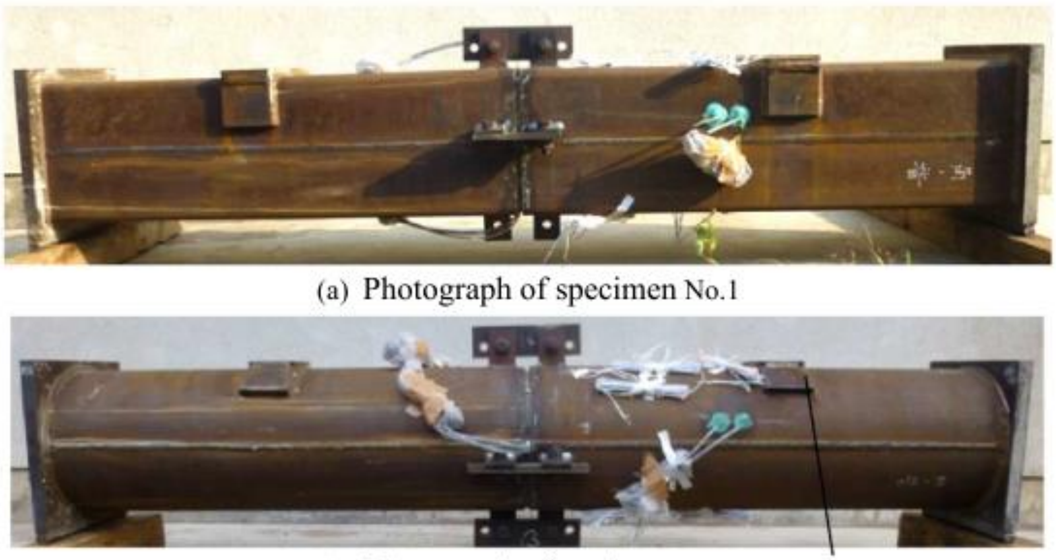

(a) Photograph of specimen No.1

(b) Photograph of specimen No.3

Fig. 4 Photographs of specimens

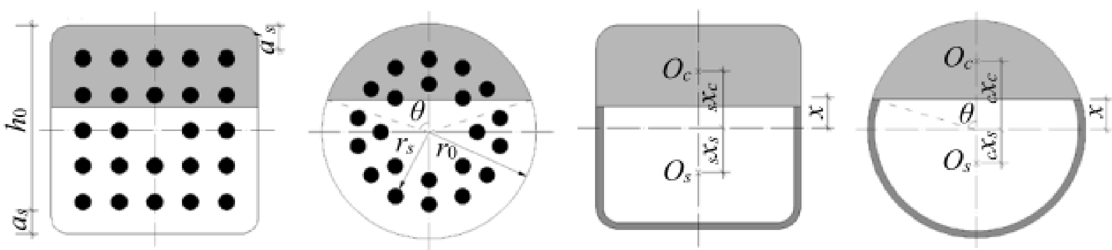

(a) Reinforced concrete section (b) Concrete filled steel tube section

Fig. 5 Stress distributions of CFST sections

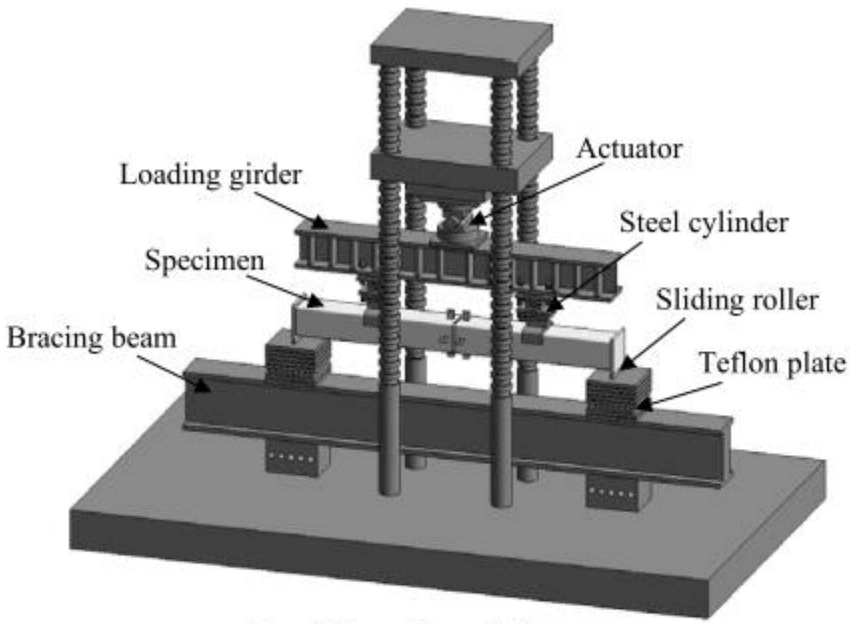

Fig. 6 Overview of the test setup

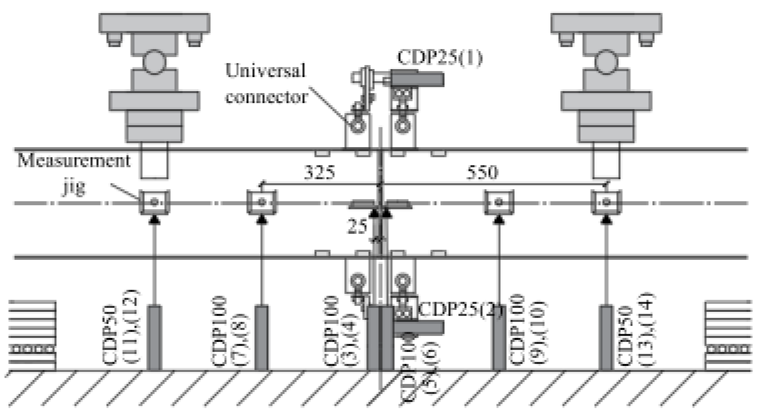

Fig. 7 Installation positions of displacement transducers

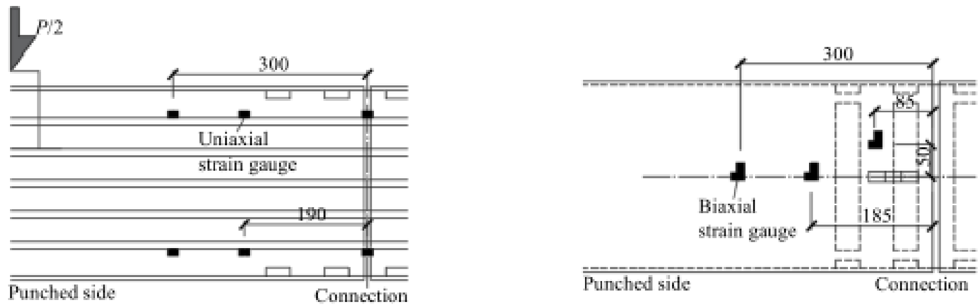

(a) Strain gauges on the rebar (elevation) (b) Strain gauges on the steel tube (plane)

Fig. 8 Arrangement of strain gauges

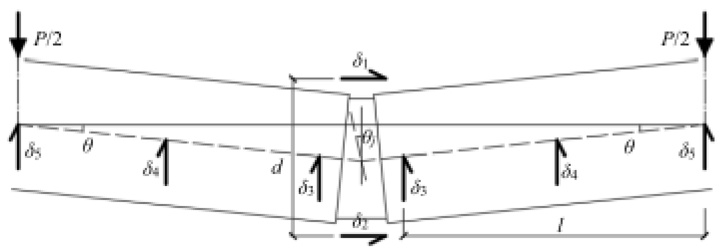

Fig. 9 The definition of flexure deformation angle (θ,θ_j)

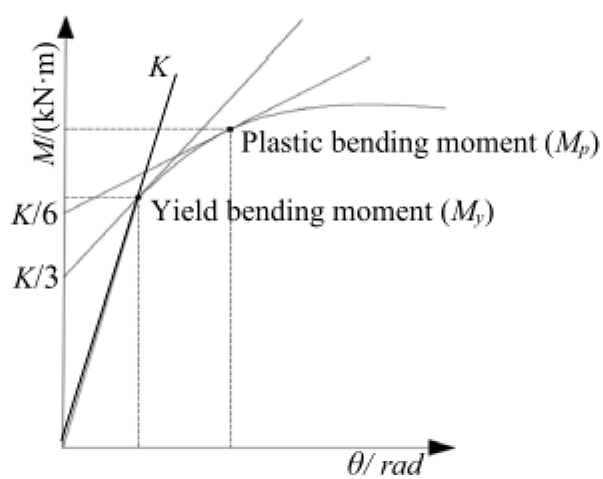

Fig. 10 Definition of key performance point

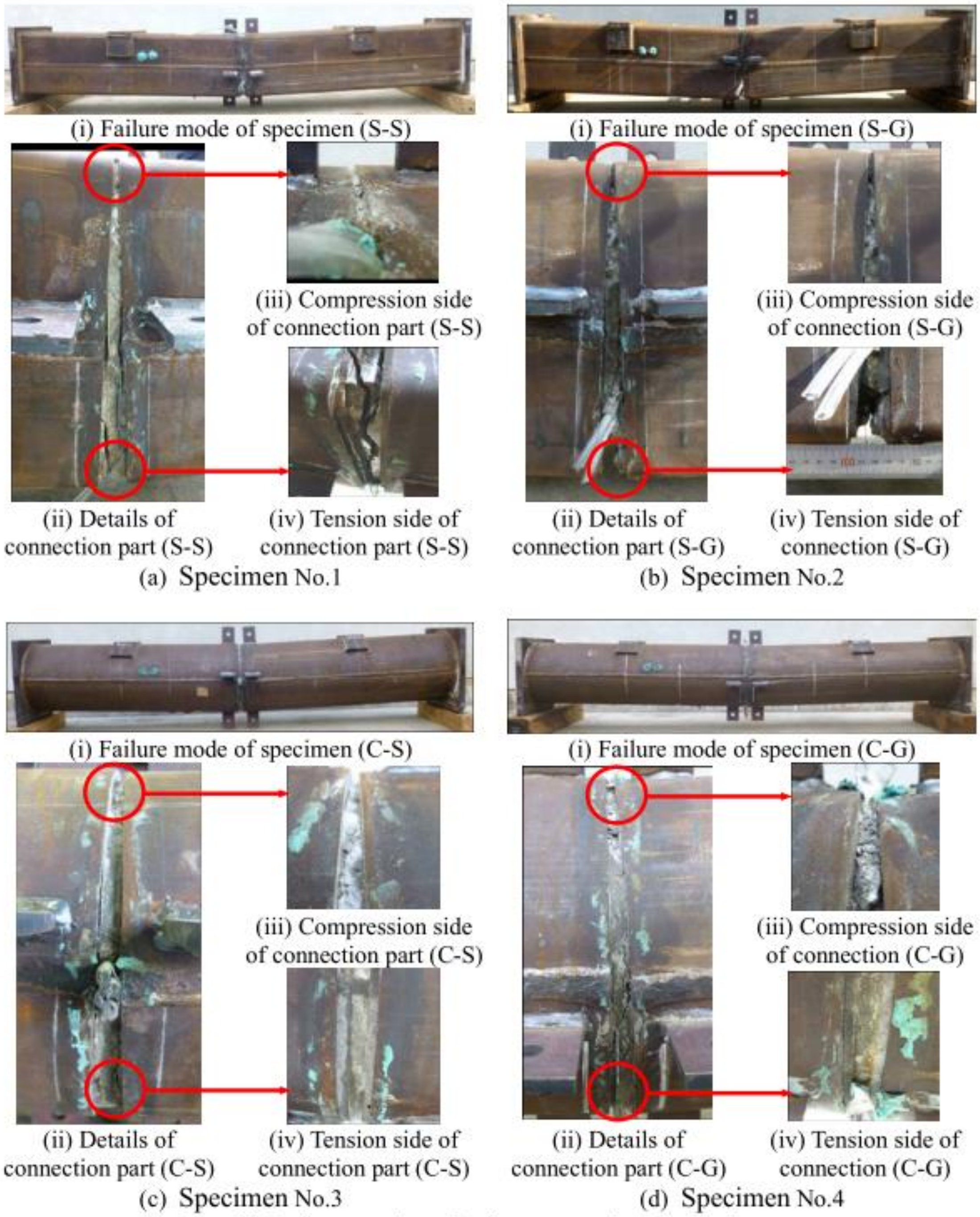

Fig. 11 Failure modes of column-to-column specimens

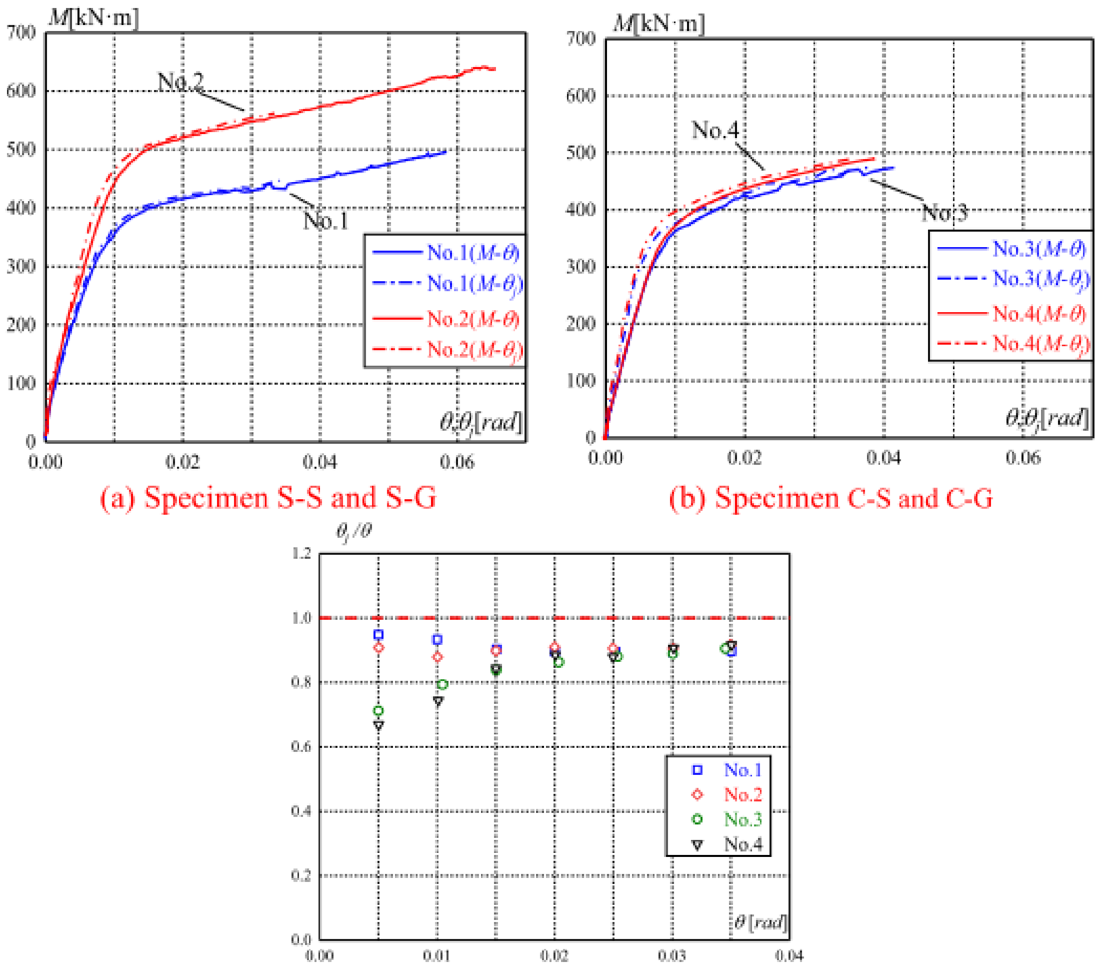

(a) Specimen S-S and S-G

(b) Specimen C-S and C-G

(c) θ_j to θ ratio

Fig. 12 $M - \theta$ or θ_j curve

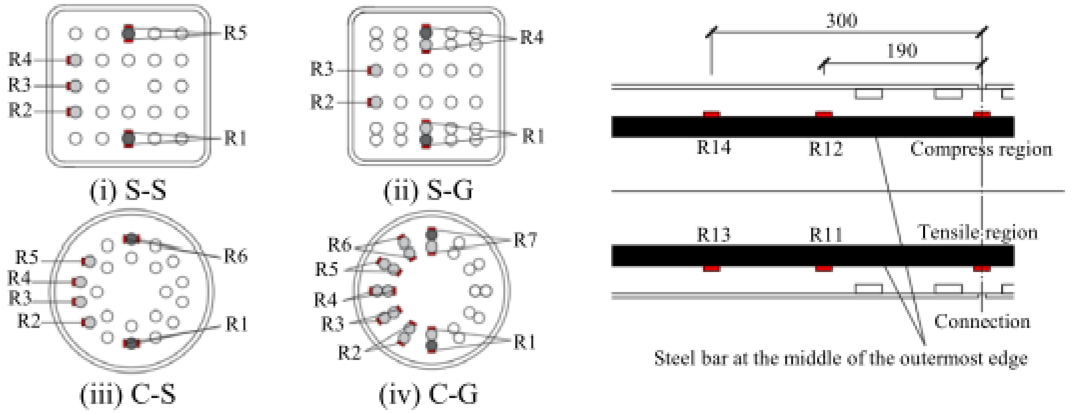

(a) Around the connection part (b) Far away from the connection part

Fig. 13 Position of strain gauges on the steel bars

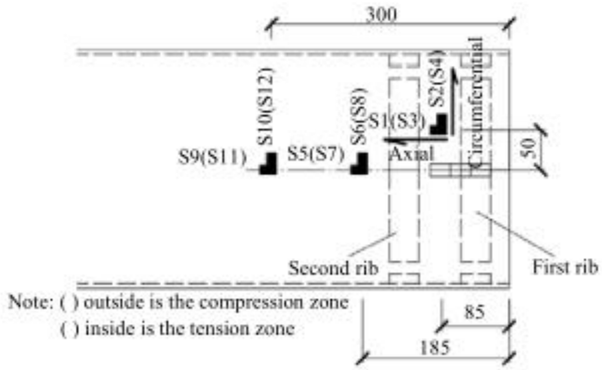

Fig. 14 Position of strain gauges on the steel tubes

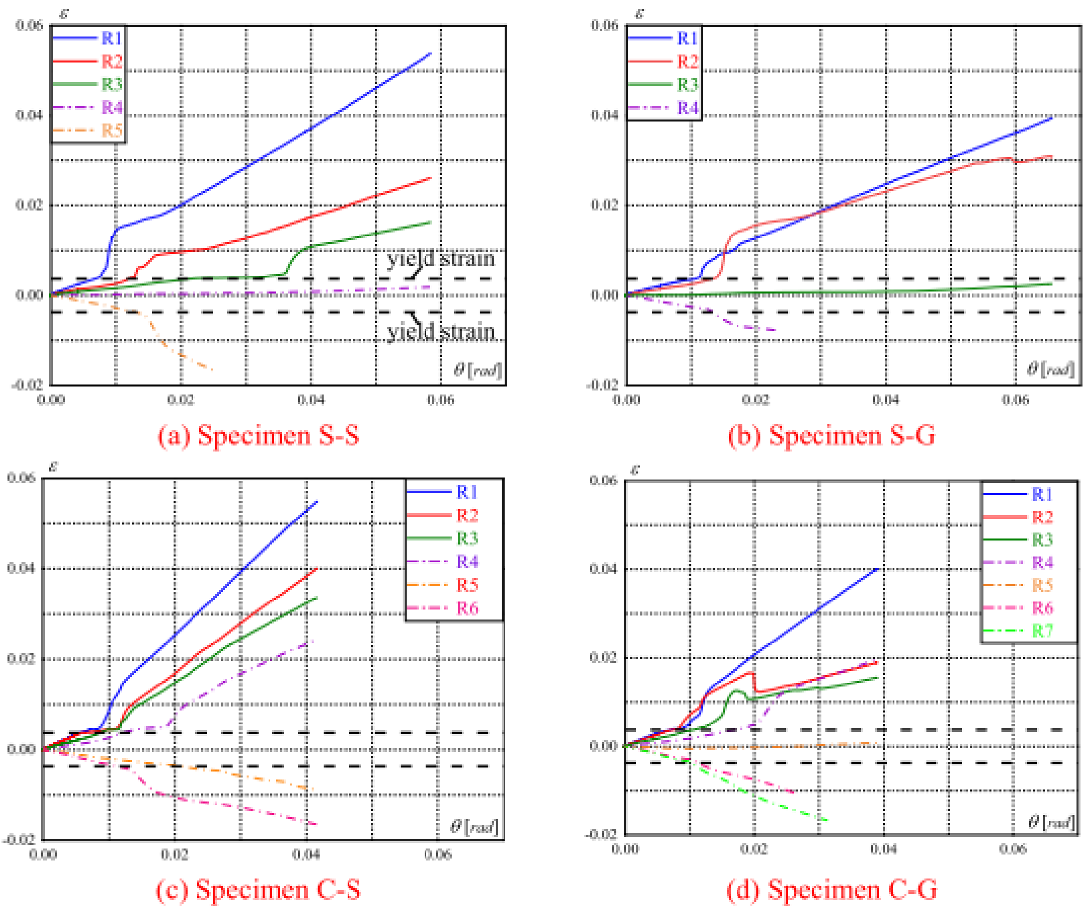

(a) Specimen S-S

(b) Specimen S-G

(c) Specimen C-S

(d) Specimen C-G

Fig. 15 ε - θ curve at the connection part of steel bars

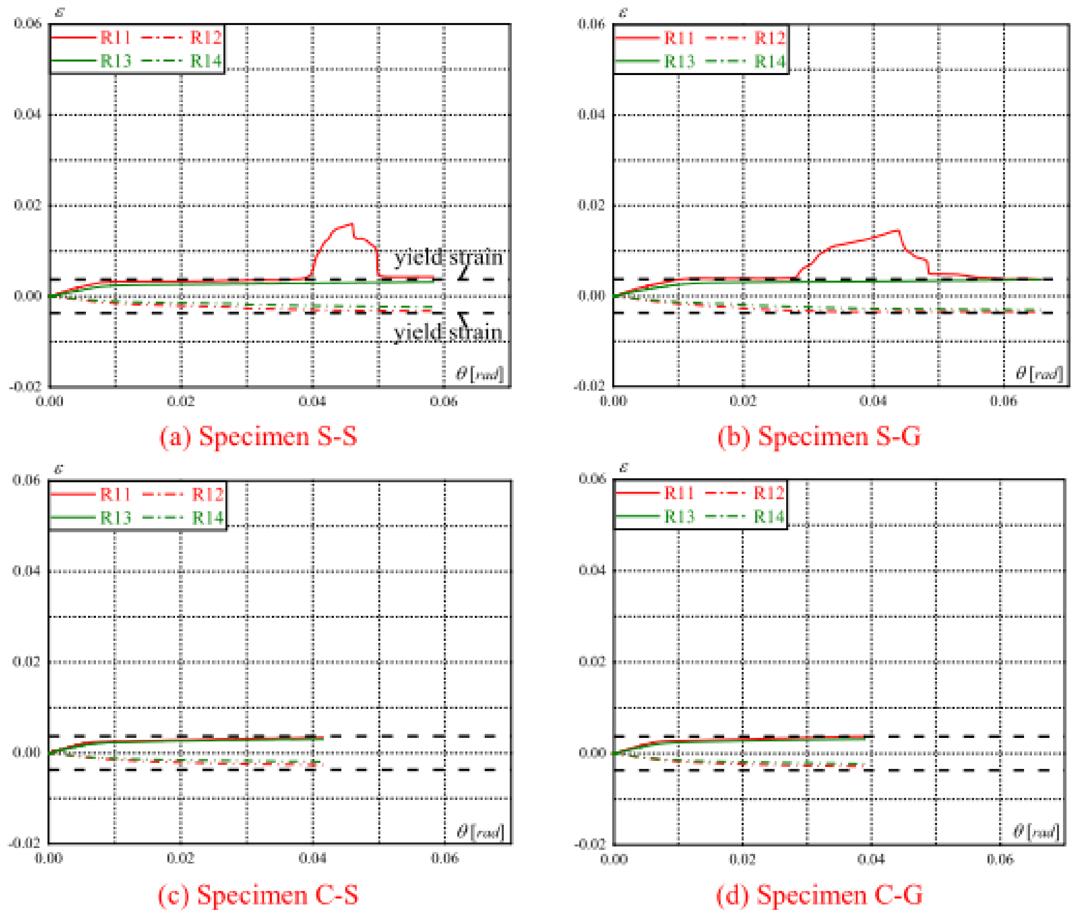

Fig. 16 ε - θ curve far away from the connection part of steel bars

538

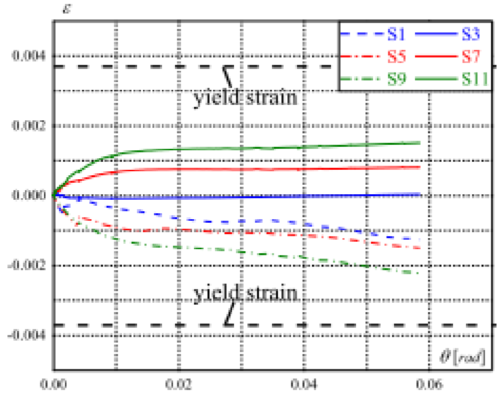

(a) An axial strain of specimen S-S

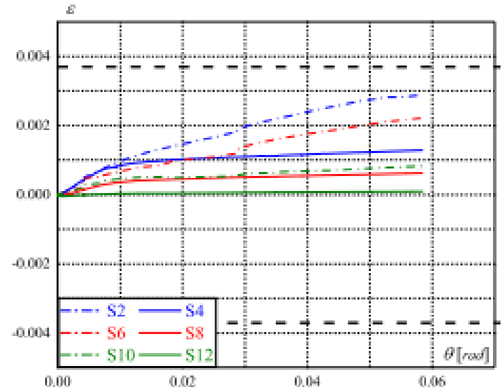

(b) A circumferential strain of specimen S-S

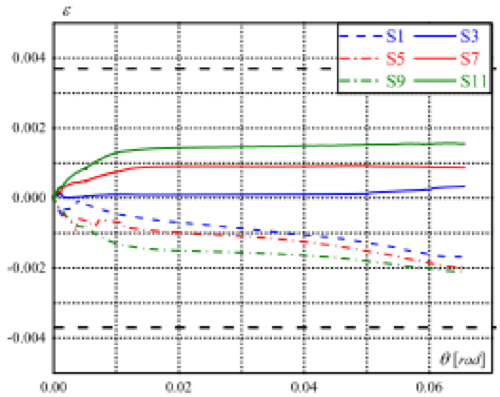

(c) An axial strain of specimen S-G

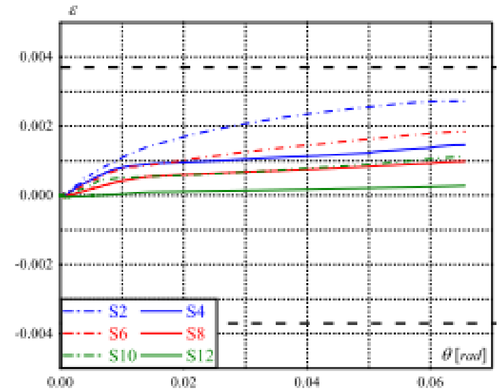

(d) A circumferential strain of specimen S-G

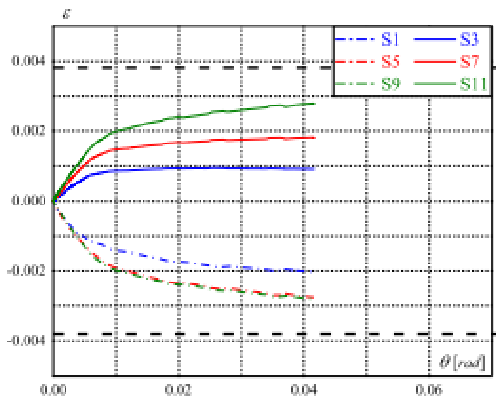

(e) An axial strain of specimen C-S

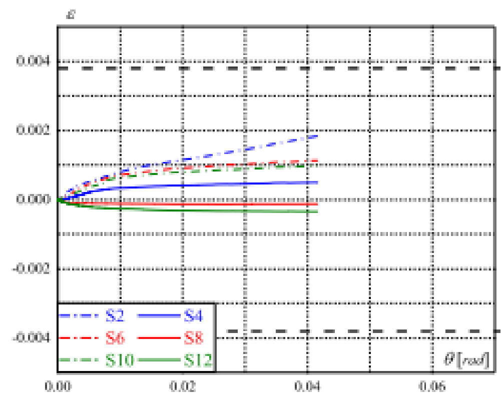

(f) A circumferential strain of specimen C-S

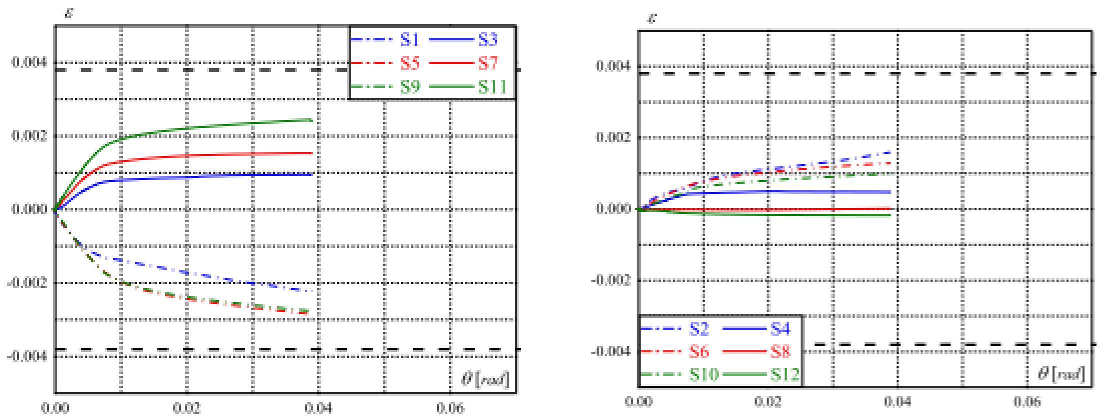

(g) An axial strain of specimen C-G

(h) A circumferential strain of specimen C-G

Fig. 17 ε - θ curve far away from the connection part of steel tubes

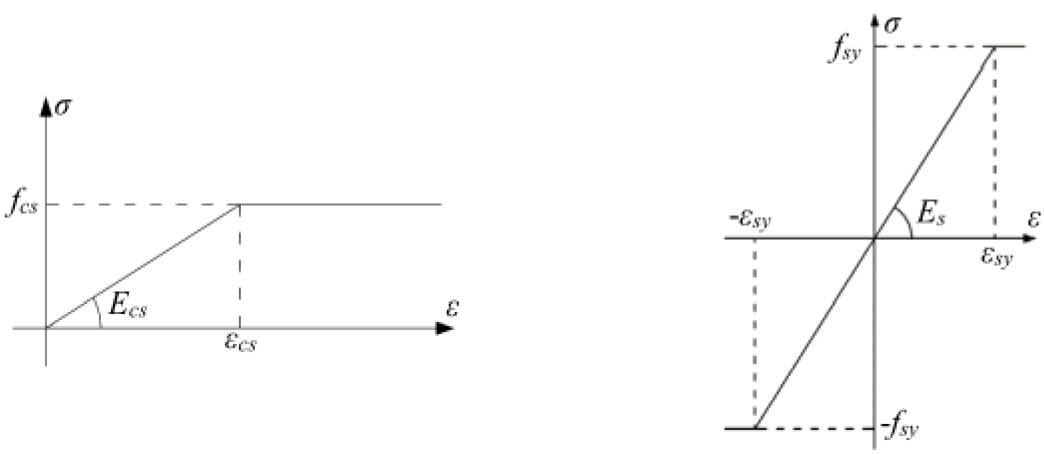

(a) Concrete

(b) Steel bar

Fig. 18 Stress (σ)-strain (ε) relationship of materials

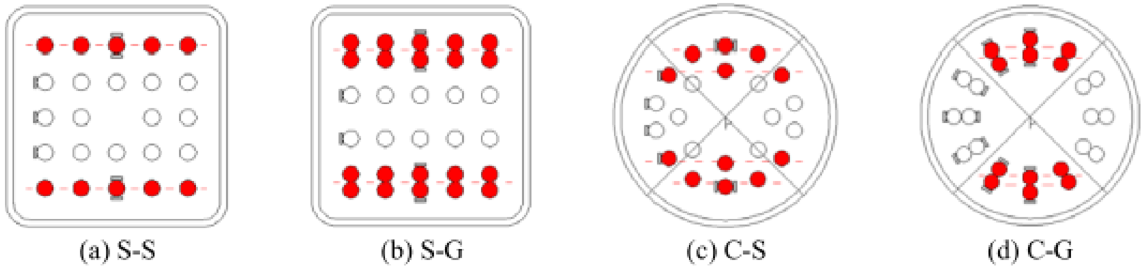

(a) S-S (b) S-G (c) C-S (d) C-G

Fig. 19 The distribution of yielding steel bars at joint

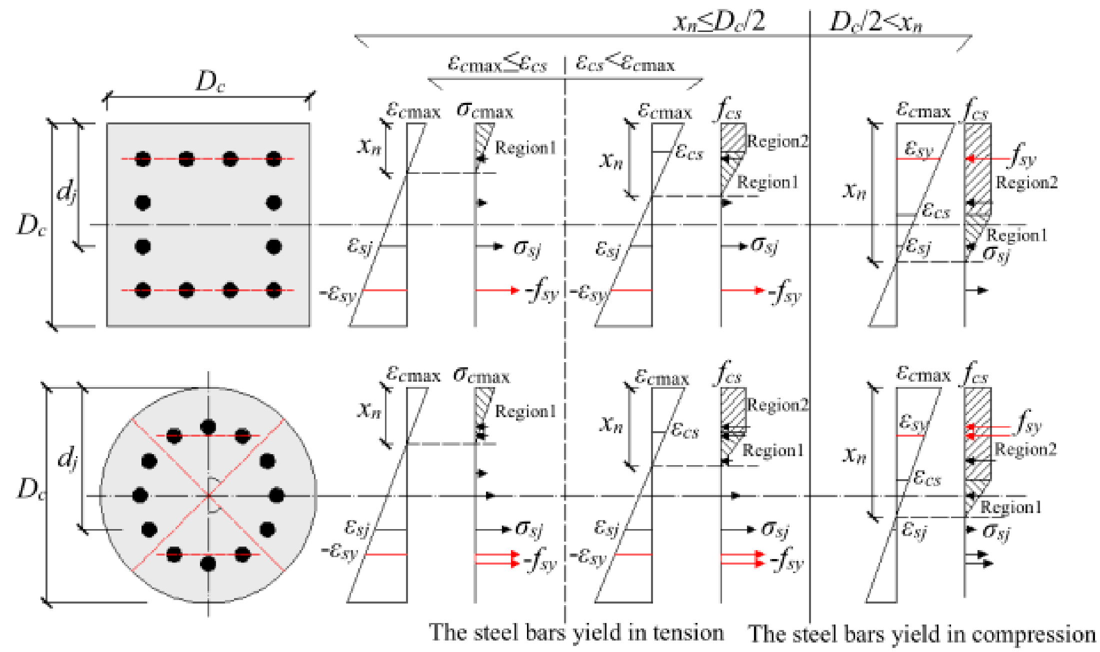

(a) Distribution of strain and stress at the yield point

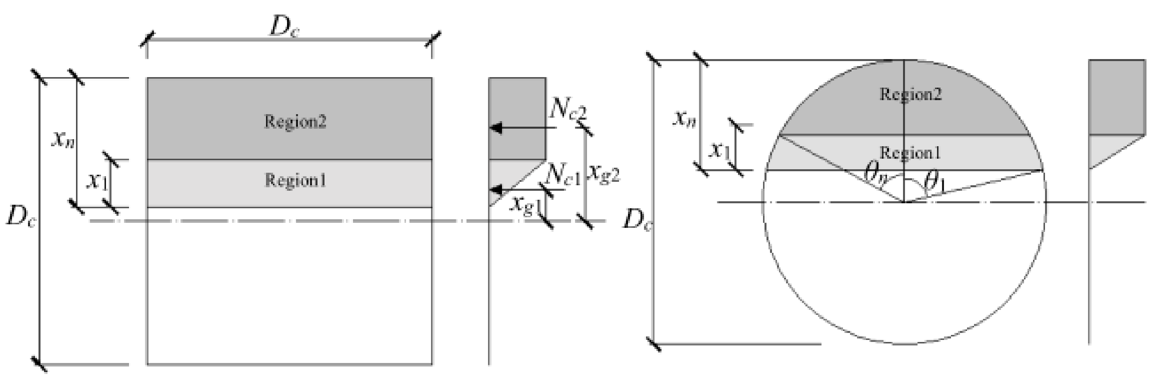

(b) Internal force distribution of concrete

Fig. 20 Schematic diagram of internal force at yield point

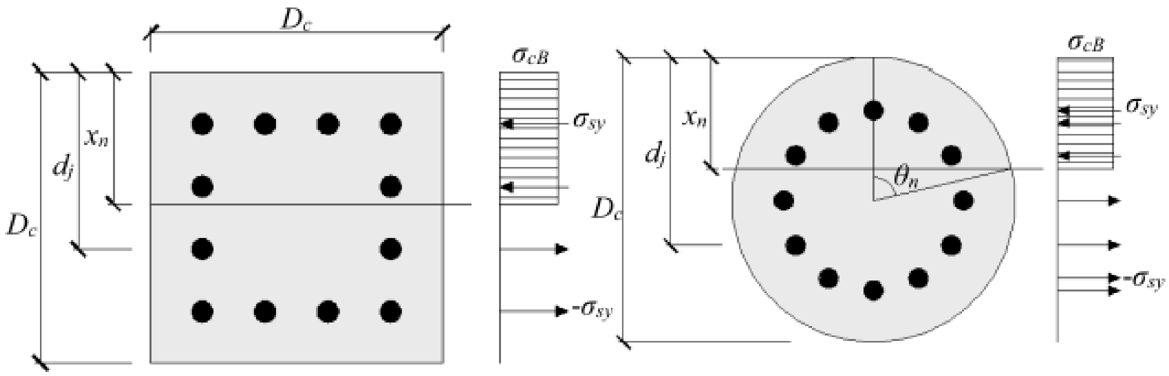

Fig. 21 Stress distribution under the ultimate stage

#

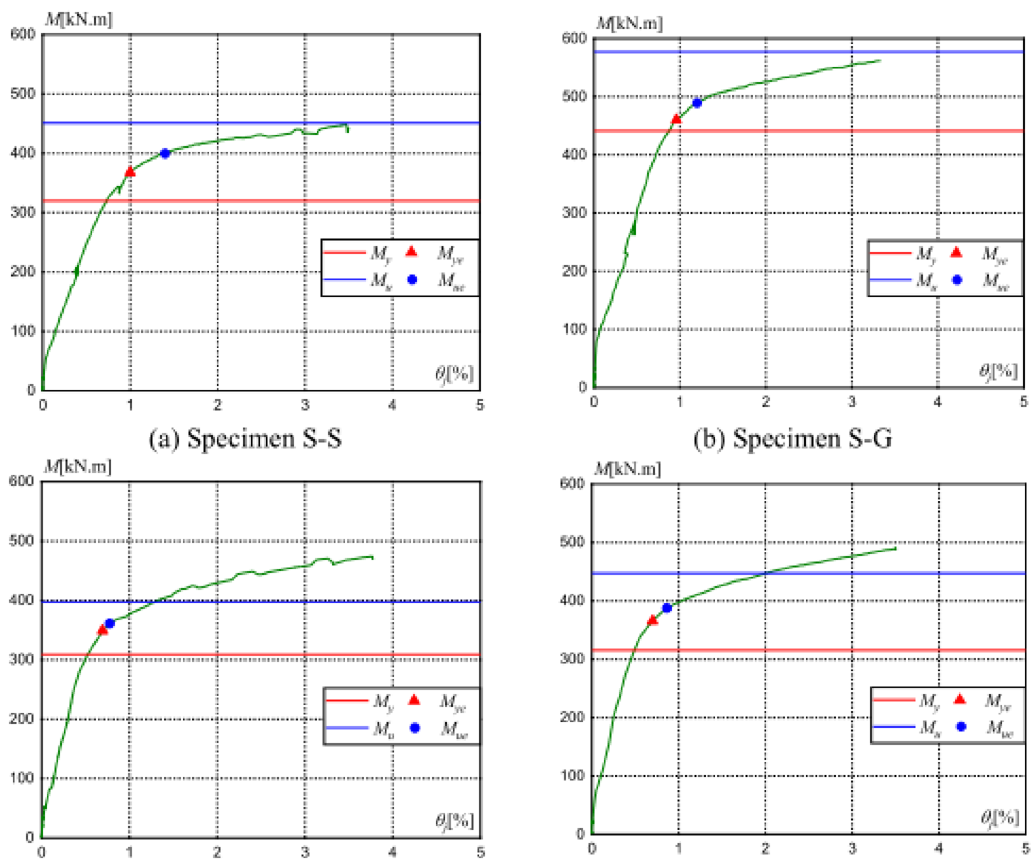

(a) Specimen S-S (b) Specimen S-G

(c) Specimen C-S (d) Specimen C-G

Fig. 22 Bending moment M - rotation angle θ_j curve at joint